Magnetic Resonance Imaging 56 (2019) 181–186

Contents lists available at ScienceDirect

Magnetic Resonance Imaging

journal homepage: www.elsevier.com/locate/mri

Original Contribution

A novel MRI phantom to study interstitial fluid transport in the glymphatic system

M.E. Komlosh[a,b], D. Benjamini[a,*], N.W. Williamson[a], F. Horkay[a], E.B. Hutchinson[b,c], P.J. Basser[a]

[a] Eunice Kennedy Shriver National Institute of Child Health and Human Development, National Institutes of Health, Bethesda, MD, USA
[b] The Henry M. Jackson Foundation for the Advancement of Military Medicine, Inc., Bethesda, MD, USA
[c] National Institute of Biomedical Imaging and Bioengineering, National Institutes of Health, Bethesda, MD, USA

ABSTRACT

The glymphatic system is a recently discovered transport system, mediated by cerebral spinal fluid (CSF), that clears metabolic and cellular waste products in the brain. This system's function in the brain is analogous to that of the lymphatic system in the rest of the mammalian body. It is hypothesized that CSF clears harmful chemicals from the brain by flowing through interstitial spaces in the brain during sleep. While there is growing recognition of the critical role the glymphatic system plays in maintaining normal brain health and in explaining pathology, there are few noninvasive imaging methods that measure and characterize the efficacy of glymphatic transport *in vivo*. In this study we designed, constructed, and tested a glymphatic transport magnetic resonance imaging (MRI) flow phantom, which combines regions that mimic CSF-filled ventricles and brain interstitial space. We tested high- and low-q space diffusion MRI and diffusion tensor imaging (DTI) acquisitions to determine if they could detect, measure, and map interstitial glymphatic flows. The results suggest that, under certain flow conditions, diffusion-weighted MRI can detect the enhanced mixing that occurs during glymphatic clearance.

1. Introduction

The glymphatic system was recently identified [1,2] as the primary drainage system of the vertebrate brain. The glymphatic system's cleansing function in the brain is analogous to that of the lymphatic system in the rest of body: the glymphatic system clears the brain by disposing of molecular and other waste products from the parenchyma. According to the proposed mechanism (Fig. 1 a.), arterial pulsation [3,4]—assisted to a lesser degree by respiration, slow vasomotion, and a cerebrospinal fluid (CSF) pressure gradient [4,5]—conducts the CSF from the subarachnoid space into para-arterial spaces. The CSF then permeates the parenchyma by transiting through pores created by aquaporin 4 (AQP4) channels on the end feet of glial cells and then migrating into the interstitial fluid (ISF) spaces. Advection of ISF also pushes debris and waste products into the paravenous space; from there the waste eventually drains into the lymphatic system. A contributor to glymphatic waste removal is the increase of the extracellular space fraction in the parenchyma during the sleep cycle [6]; this activity allows more CSF to enter this compartment and wash away the toxic metabolites and debris that accumulate there during the wake cycle.

A well-functioning glymphatic system is required to maintain a healthy vertebrate brain. It has been shown that in an aging brain, the activity of the glymphatic system is dramatically reduced [7]; this reduction correlates with the increased risk of developing neurodegenerative diseases. Indeed, in many neurodegenerative diseases, such as Alzheimer's [8] and Parkinson's diseases [9], toxic protein debris accumulates in the parenchyma. Another major risk factor in developing brain pathologies is traumatic brain injury (TBI) [10,11]. Brains studied postmortem that have sustained a single or repetitive sports injuries—mild or severe—or moderate to severe blast or battle injuries, show an accumulation of tau proteins, a marker for TBI. Clearly, understanding the glymphatic system's transport mechanisms is crucial for understanding sequelae of TBI and other neurodegenerative diseases and possibly detecting and diagnosing transport anomalies shortly after they happen.

Aspects of the glymphatic system that have not been well studied, particularly in humans, are reliable estimates of the velocity and volume flow rates associated with CSF migration through the parenchyma. This dearth of data has hampered the development of realistic theoretical and computational models of glymphatic clearance and has made it challenging to determine whether imaging methods, such as magnetic resonance imaging (MRI) velocimetry, could be used to assess glymphatic clearance. Molecular tracer studies, combined with histology and mathematical models of porous flow in rat brain [12–15], have been extrapolated to predict a range of CSF flow rates in human tissue of 0.13 to 0.39 ml/min [16].

Diffusion-weighted MRI (DW-MRI) methods [17–19], which are sensitive to net water displacements, are a prime candidate for detecting CSF flow through the parenchyma. In this type of experiment, a pair of pulsed-field gradients, the first to encode and the second to

* Corresponding author.
E-mail address: dan.benjamini@nih.gov (D. Benjamini).

https://doi.org/10.1016/j.mri.2018.10.007
Received 17 September 2018; Received in revised form 13 October 2018; Accepted 14 October 2018
0730-725X/ Published by Elsevier Inc.

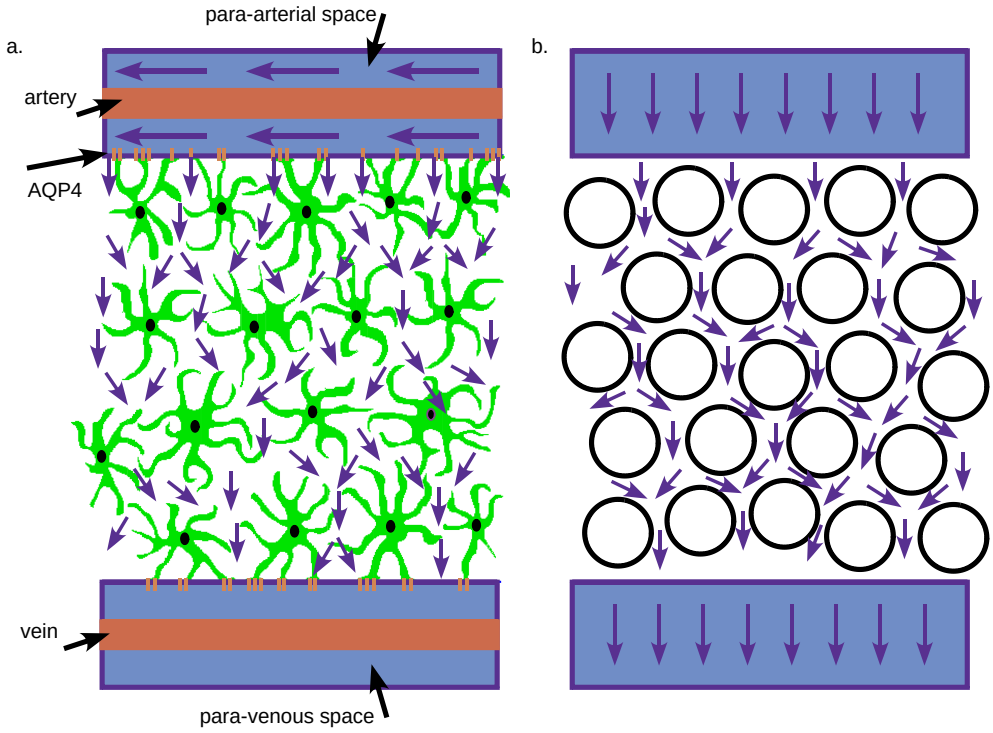

Fig. 1. a. Schematic illustration of the glymphatic flow through the parenchyma. CSF water from the para-arterial space enters the parenchyma *via* the AQP4, which is situated on the glial cell end feet, creating convection flow in the direction of the para-venous space. b. Schematic illustration of the water flow through the phantom. The phantom's bead layer, comprising beads of 10 μm diameter, simplifies the complex nature of the parenchyma. Constant water flow causes convection that simulates the dispersion process that occurs in the glymphatic system.

refocus the magnetization, separated by diffusion sensitizing time (Δ), is used. By Fourier transforming the signal profile resulting from stepping up the gradient strength, the propagator, $P(R,\Delta)$, is measured from the signal, $E(q,\Delta)$ [20],

$$E(q,\Delta) = \int P(R,\Delta)e^{i2\pi qR}dR, \quad (1)$$

where $q = \gamma g\delta/2\pi$, γ is the magnetogyric ratio, g is the gradient amplitude, and δ is the gradient pulse duration. The propagator is the water displacement probability density function, which indicates the likelihood for particles to undergo net displacement, *R*. From the low-q values echo attenuation, the diffusion coefficient (which under convective flow becomes the dispersion coefficient due to the water advection) can be calculated.

All evidence for glymphatic flow so far has been based on *in vivo* and *ex vivo* tissues (*e.g.*, [21]). Estimating the flow rates through the parenchyma in such studies has been difficult due to the complexity of the tissue, which consists of neurons and glia cells. Using MRI to study glymphatic flow is particularly difficult because the parenchyma dimension (with a depth of approximately 200 μm) is smaller than the *in vivo* MRI voxel resolution. In order to study the flow characteristics of the glymphatic system and the feasibility of measuring glymphatic flow and transport in tissue, it is prudent to study a simplified but fully characterized phantom first, as has been done in other MR applications [22–26]. In this study, we report the design, development, and testing of a novel MRI phantom that possesses salient features of brain parenchyma. We tested high- and low-q space diffusion MRI as well as diffusion tensor imaging (DTI) acquisitions to determine if they could detect, measure, and map interstitial glymphatic flows.

2. Materials and methods

An MRI phantom used to model glymphatic flows was prepared as follows: polystyrene microspheres with a 10.03 ± 0.09 μm diameter (Duke Standards, 4000 Series Monosized particles, Thermo Scientific) were packed in water in a 5-mm inner diameter Tricon 5/100 Column (GE Healthcare), creating a randomly packed bed (representing brain parenchyma) with a water zone above (representing a CSF-filled para-arterial space) (Fig. 1b.). The bead diameter was chosen to represent a characteristic length scale in the parenchyma. The porosity (ϕ) of the loosely packed beads was determined to be ~0.44, which agrees with the literature [27]. The column was placed inside a Bruker 7 T vertical wide-bore magnet with an AVANCE III spectrometer equipped with a micro2.5 gradient set and three-axis GREAT 60 amplifiers resulting in a nominal gradient strength of 24.92 mT m^{-1} A^{-1}.

A peristaltic pump (Pharmacia Biotec) circulated water from the top of the column through the bead pack (Fig. 2). Three mean flow rates were chosen: 0.041, 0.44, and 0.88 ml/min. These flow rates are, respectively, significantly lower than the estimated value for glymphatic clearance, close to the value reported for the convective flow of the glymphatic system, and double the reported value. For our phantom geometry, these flow rates correspond, respectively, to the mean velocities of 35, 371, and 747 μm/s in the bulk layer. The flow rate in the bead layer, $\langle v\rangle$, was estimated to be $\langle v_{bulk}\rangle/\phi$ [28], which resulted in velocities of 79, 843, 1698 μm/s, respectively. The velocities of the bead pack correspond to the Péclet number, which is the ratio between the mass transport *via* convection and diffusion ($Pe = \langle v\rangle d/D_0$), of 0.31, 3.31, and 6.67, where d = 10 μm (bead diameter) and D_0 = 2000 μm/s^2. It is worth noting that only the last two flow rates, which resulted in $Pe > 1$, are expected to show dispersive behavior.

A DWI echo-planar imaging (EPI) sequence was applied with the following parameters: echo time (TE)/repetition time (TR) = 59/3000 ms, 8 segments, two 2-mm axial slices (one for the bulk layer and the other for the bead pack) with spatial resolution = 125 × 125 μm^2; diffusion sensitizing gradients were applied in the directions parallel (z-direction) and perpendicular (x-direction) to the flow, with a gradient pulse duration of δ = 3 ms, separation of Δ = 50 ms, and 41 q-values from 0 to 53.6 mm^{-1}. Flow propagators were calculated by applying a fast Fourier transformation (FFT) to the resulting real and imaginary data using MATLAB (The MathWorks, Natick, MA). The apparent diffusion coefficients (ADC) or dispersion coefficients, Dx and Dz, were calculated from the low-q data (G_{max} = 160 mT m^{-1}, q_{max} = 20.44 mm^{-1}).

Because our aim was to test the phantom with methods routinely used *in vivo*, DTI data for the reported biological flow rate (0.44 ml/min) were acquired by using the MRI acquisition parameters as above

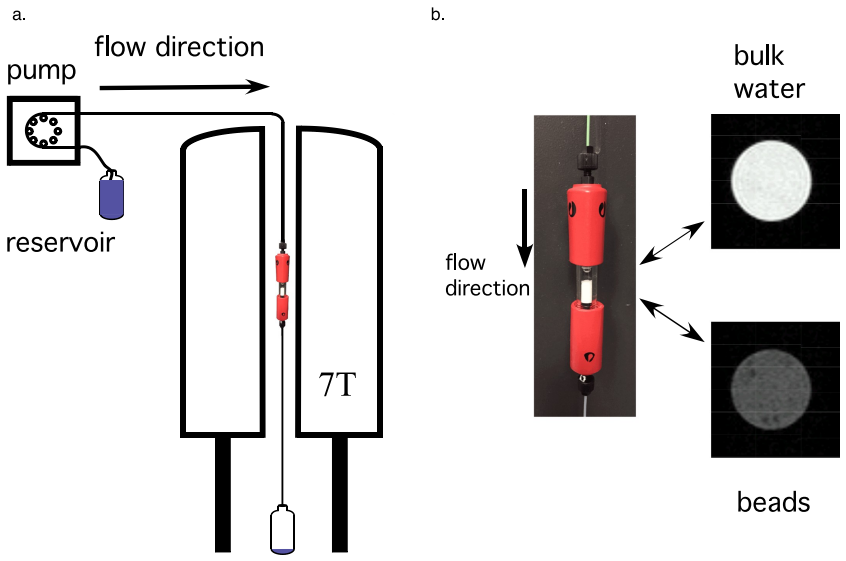

Fig. 2. The MRI flow system consists of a. a peristaltic pump that produces flow though the column, which is placed in the 7 T magnet. b. A magnification of the GE column packed with a layer made up of 10 μm beads (parenchyma) and a free water layer (para-vascular space), along with T_2-weighted images from the bead and bulk layers, respectively.

with two diffusion acquisition protocols: (1) $\Delta = 50$ ms, $\delta = 3$ ms, b-values = 400 and 800 s/mm^2 with 21 gradient orientations. ADCs parallel (D_{zz}) and perpendicular (D_{xx}) to the flow direction, mean diffusivity (MD), and fractional anisotropy (FA) [19] were calculated. (2) To observe time dependency of the dispersion coefficient, two diffusion observation times, $\Delta = 25$ and 50 ms, pulse duration of $\delta = 3$ ms, and seven linearly sampled b-values in the range of 0 to 600 s/mm^2 with 21 gradient orientations were used. ADCs parallel and perpendicular to the flow direction were calculated from the DWI signal attenuation data.

3. Results and discussion

We first performed a detailed analysis of the water displacement distributions by observing the full q-space propagators under the different experimental conditions. This analysis was designed to establish the validity of the phantom system and the flow regime in these experiments. Fig. 3 shows the resulting propagators; the longitudinal propagator, $P(Z,\Delta)$; and the transverse propagator, $P(X,\Delta)$, at the three flow rates and without flow. Fig. 3a. and c. correspond to the bulk layer; Fig. 3b.and d. correspond to the bead layer. The theoretical mean displacements in the flow direction (R_{mean}) at the experimental observation time, $\Delta = 50$ ms, were 1.75, 18.5, and 37.3 μm for the bulk layer, and 3.95, 42.1, and 84.9 μm for the bead layer, at flow rates of 0.041, 0.44, and 0.88 ml/min, respectively. These theoretical values agree with the displacements presented in Fig. 3. The bulk layer $P(Z,\Delta)$ exhibited the expected Poiseuille velocity profile, indicated by the Gaussian propagator (Fig. 3a., dotted line), which is shifted to the right as the flow rate increases [29]. $P(X,\Delta)$ as a function of flow rate exhibited the expected water diffusion profiles for all flow rates (Fig. 3c.), namely, broadening in the bead layer (due to dispersion) and unchanged in the bulk water layer. $P(Z,\Delta)$ of the bead layer deviated from a Gaussian profile, as expected: an increasingly wider profile and bigger shift in net displacement for the two lower flow rates and an asymmetric profile for the highest flow rate. All displacement profiles from the bead layer displayed enhanced flow due to the dispersive mixing process. Note that $P(Z,\Delta)$ at the lowest flow rate (0.041 ml/min) in the bead layer exhibited a slight, albeit detectable, shift in the displacement profile, which demonstrates the sensitivity of full q-space diffusion-weighted approaches to detecting low flow rates.

Propagator measurements are particularly sensitive to detecting displacements in the low-flow regime, which low-q measurements are not expected to detect. However, measuring the propagator requires applying strong gradients to acquire the entire q-space and, in addition, dense signal sampling. These conditions are difficult to achieve in preclinical and clinical spectrometers in which both gradient strength and acquisition time are limited. It has been suggested recently that an analytical representation of the signal could be used instead of an FFT to reconstruct the propagator [29]. The analytical method was shown to be robust to partial data acquisition and demonstrated better low-flow detection sensitivity than the FFT-based method.

A more accessible alternative to measuring the propagator would be to estimate the low-q dispersion coefficient. Table 1 presents these coefficients (longitudinal and transverse) obtained from the low-q regime ($q_{max} = 20.44$ mm^{-1}) data; only a single gradient direction was used in each case (*i.e.*, not a full DTI acquisition). In the no-flow case, the ADCs in the bead section indicated isotropic diffusion, and the bulk water layer diffusivity was at the expected value for free diffusion at the temperature of the experiment. With flow conditions, all of the measured coefficients were in agreement with the expected dispersion values for the calculated Péclet numbers [19]. Because the bead packing order is known, and the acquired data can be predicted, these findings serve as a calibration measure to assure our phantom can be used to study the glymphatic system using MRI. The dispersion coefficients at the lowest flow rate of 0.041 ml/min did not differ from the diffusivity without flow in both the bead and bulk layers, indicating that low-q DWI measurements are not sufficiently sensitive to detect such low flow rates. This, indeed, was also expected because the lowest flow rate ($Pe < 1$) is at the diffusion-dominated regime, which makes its detection and separation from a coherent flow very challenging. In the biologically relevant flow rate (0.44 ml/min), Dz in the bulk layer exhibited a diffusivity similar to the value detected without flow. In the bead layer, however, both Dx and Dz showed significant increases of over 145% and 62%, respectively, compared with the diffusivities obtained without flow. This finding suggests that the non-uniform velocity distribution within the interstices of the bead pack increases dispersive mixing as measured by the increase in the ADC.

Of greatest interest is the increase of dispersive mixing observed in the direction perpendicular to the direction of the main flow, *i.e.*, transverse dispersion. When ADC is measured in tissue or in *in vivo* samples, the flow direction is expected to be randomly oriented within the MRI voxel resolution; thus, coherent flow would be harder to detect. The transverse ADC in the bead region gives us an insight into the expected results in the case of microscopically, randomly oriented tissue. At the highest flow rate (0.88 ml/min) both layers (bulk and bead) exhibited a significant increase in diffusivity, indicating that for high flow rates, the low-q ADC measurement can detect both the increased mean velocity of the bulk layer and the dispersive mixing in the bead layer. However, it would be prudent to say that this flow rate is not

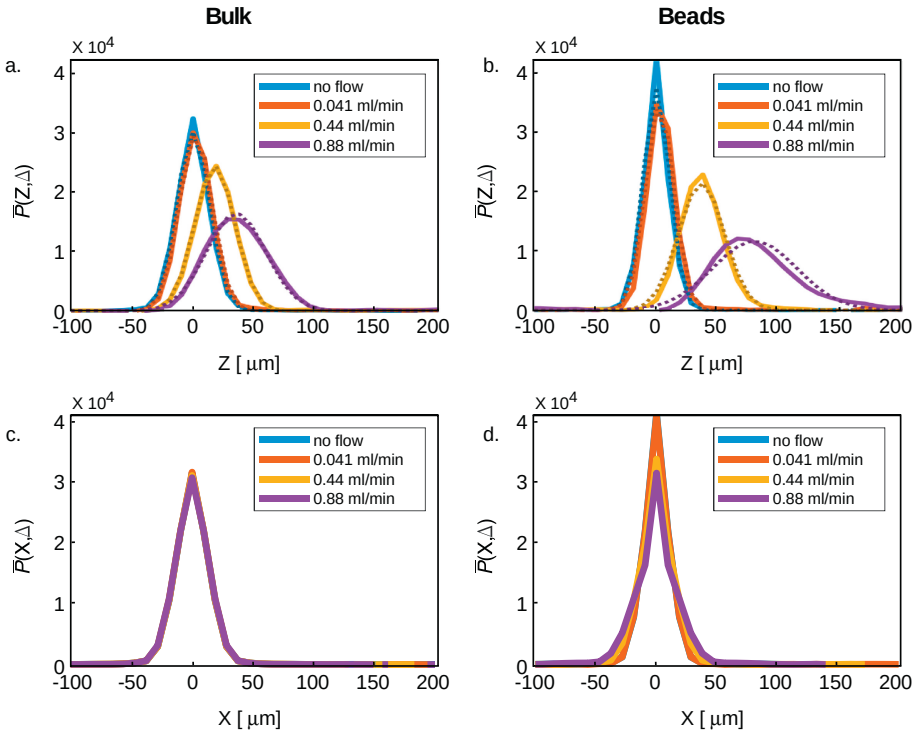

Fig. 3. Displacement propagators parallel, $P(Z,\Delta)$, and perpendicular, $P(X,\Delta)$, to the flow direction, at three flow rates and without flow. a. and c. are the bulk layer, and b. and d. are the bead layer. Gaussian propagators are superimposed over $P(Z,\Delta)$ (dashed line).

Table 1
ADCs parallel (Z) and perpendicular (X) to the flow direction of the phantom's bulk and bead layers for different flow rates. The presented coefficients were averaged across a region of interest (ROI) at the center of the tube, along with their standard deviations.

ADC [x10^{-3} mm^2/s]	Beads		Bulk	
Flow [ml/min]	Dx	Dz	Dx	Dz
0	1.29	1.24	2.00	1.96
0.041	1.36	1.26	1.99	1.94
0.44	2.09	3.04	2.00	2.02
0.88	2.78	9.3[a]	2.06	3.50

[a] Coefficient was obtained from fitting the attenuation curve up to b = 270 s/mm^2 due to rapid signal loss. The standard deviation (SD) of this measurement was 0.30 × 10–3 mm^2/s. SDs in all other measurements were smaller than the reported least significant digit.

expected in the glymphatic flow case. Note that the Dx value is similar to D_0 for the bulk flow for all flow rates, indicating the observed dispersion is indeed a result of a mixing process in the bead layer.

Focusing on the most biologically relevant flow rate (0.44 ml/min), standard DTI acquisition and processing protocols were used. This approach, which is readily available in preclinical and clinical scanners, would be more feasible for detection of flow *in vivo* despite the limitations on the detection of low flow rates. Figs. 4 and 5 show the FA, Dxx, Dzz, and MD maps for 0 and 0.44 ml/min flow rates, along with the corresponding mean metrics calculated from a circular region of interest (see Table 2). In all cases of the bulk water region, the DTI parametric maps appear to be uniform. The FA values in the bulk water layer point to isotropic diffusivity, while the MD derived from the flow measurement is slightly higher compared with no flow (Fig. 4a. and c.). Conversely, microstructural heterogeneity is evident in the bead layer; this heterogeneity is most pronounced in the FA map with no-flow conditions (Figs. 4b. and d.). In particular, local, high-intensity FA

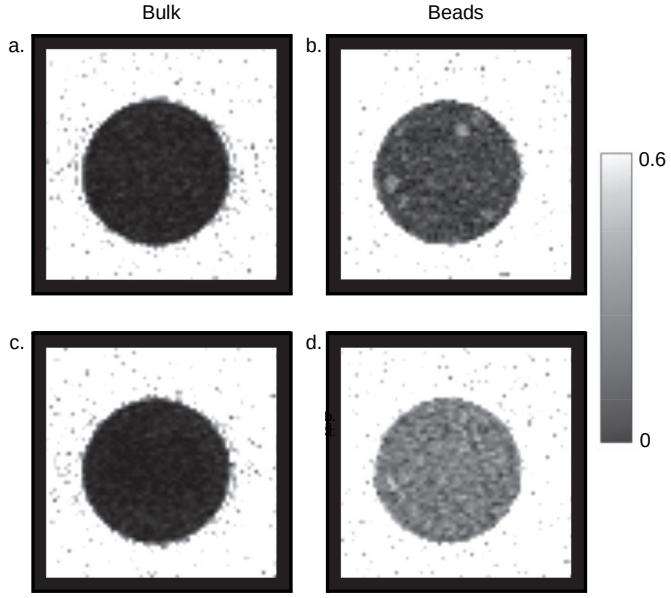

Fig. 4. DTI FA maps of the bulk (a,c) and bead (b,d) layers. a and b: no flow. c and d: flow rate of 0.44 ml/min. Mean FA values are reported in Table 2.

values, which are markers for anisotropy, indicate a non-uniform packing of the beads (and hence, non-uniform pore shapes). Mean values for all DTI metrics were greatly increased due to the introduction of flow to the bead layer. As a result of voxel resolution that is comparable to the parenchyma size (approximately 200 μm), it is highly unlikely pure coherent flow would be detected. With such resolution, two scenarios are likely: (1) a completely randomly oriented tissue on the voxel scale, which in our phantom system is mimicked by the transverse direction or (2) voxels that include a partial volume of coherent flow (such as a blood vessel) and incoherent (parenchyma) motion, a

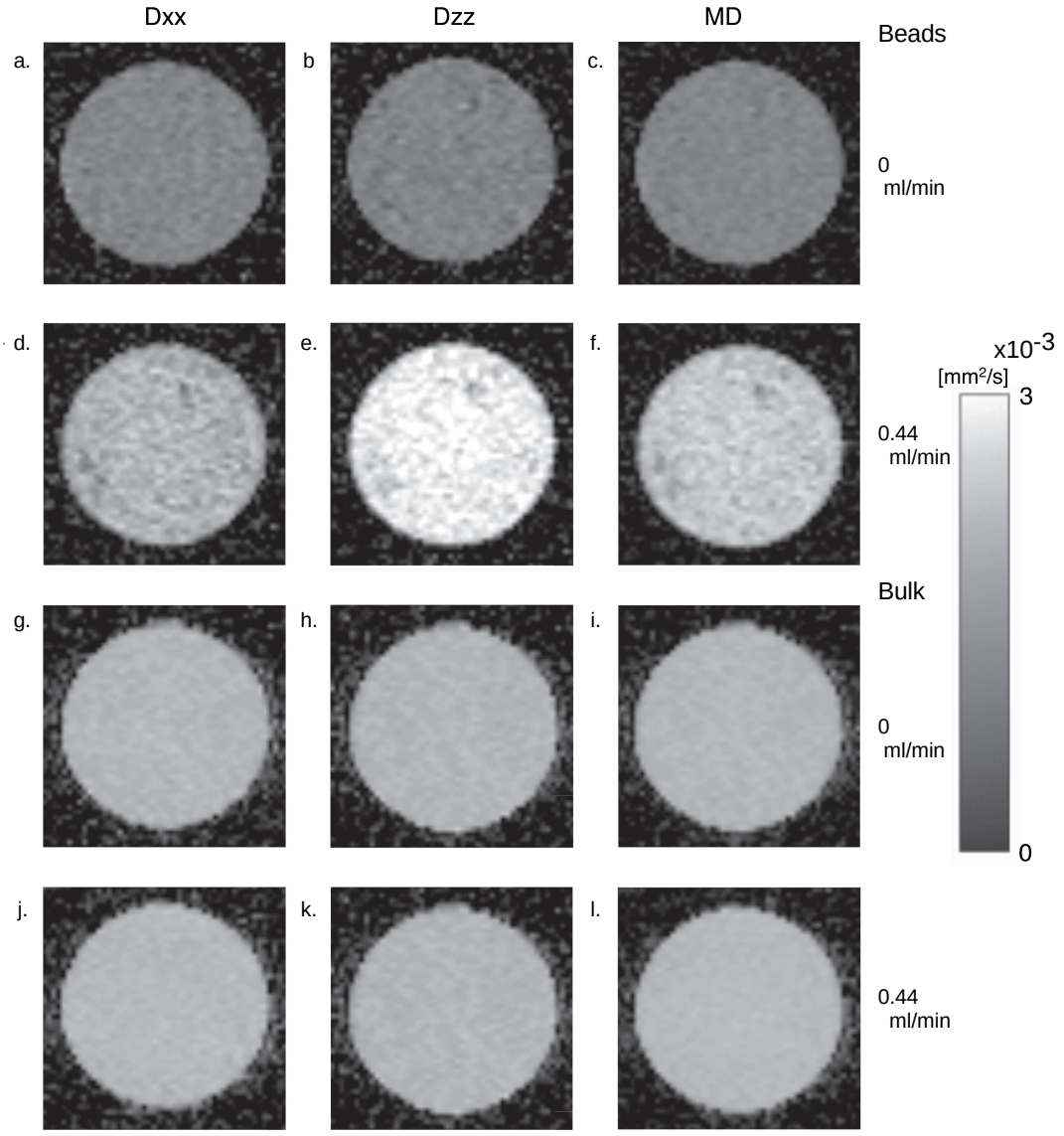

Fig. 5. DTI ADC and MD maps of the bead (a–f) and bulk (g–l) layers. a–c. and g–i:no flow. d–f and j–l: flow rate of 0.44 ml/min. Mean values are reported in Table 2.

scenario in which FA and MD parameters may be more suitable candidates to focus on.

A slightly different DTI acquisition protocol (the second protocol in the Materials and Methods section) was used to test the time dependency of the dispersion coefficient in this system as a function of the observation time, Δ. Table 3 shows that the longitudinal and transverse dispersion processes in the bulk region and transverse dispersion in the bead region do not depend on the observation time. This means that, in those cases, the fluid probed the entire heterogeneity of the system during the observation period. However, in the case of the longitudinal dispersion in the bead region we can see a clear time dependency, which is consistent with results from Khrapitchev and Callaghan [30].

Table 3
ADCs parallel (Z) and perpendicular (X) to the flow direction of the phantom's bulk and bead layers for a flow rate of 0.44 ml/min at different observation times. The presented coefficients were averaged across an ROI at the center of the tube, along with their standard deviations.

ADC ± SD [x10^{-3} mm^2/s]	Beads		Bulk	
Δ [ms]	Dxx	Dzz	Dxx	Dzz
25	1.92 ± 0.07	2.90 ± 0.10	1.95 ± 0.02	2.04 ± 0.05
50	1.90 ± 0.11	3.20 ± 0.21	1.94 ± 0.03	2.08 ± 0.07

Table 2
DTI metrics for 0 and 0.44 ml/min flow rates. The presented coefficients were averaged across an ROI at the center of the tube, along with their standard deviations.

ADC ± SD [x10^{-3} mm^2/s]	Beads				Bulk			
Flow [ml/min]	FA	Dxx	Dzz	MD	FA	Dxx	Dzz	MD
0	0.11 ± 0.05	1.20 ± 0.11	1.20 ± 0.12	1.24 ± 0.08	0.05 ± 0.01	1.92 ± 0.06	1.90 ± 0.07	1.92 ± 0.05
0.44	0.24 ± 0.05	1.90 ± 0.22	2.60 ± 0.30	2.10 ± 0.21	0.04 ± 0.01	1.94 ± 0.05	1.97 ± 0.06	1.95 ± 0.04

They showed that observation times > 10 times the correlation time to flow one bead diameter (defined as $d/\langle v \rangle$) are needed for fluid dispersion to become a completely Gaussian, stochastic, and irreversible process. In our case, that would mean that the measured longitudinal dispersion coefficient would reach an asymptotic value for $\Delta > 120$ ms. Additionally, they showed that much less time is required to reach this limit for dispersion perpendicular to flow; this finding is in agreement with the measured apparent asymptotic transverse dispersion at $\Delta = 50$ ms. As previously mentioned, given *in vivo* MRI spatial resolution and the expected tissue microstructure, glymphatic flow would most likely appear as isotropic dispersion, which is mimicked by the transverse flow in the bead region. Our Dxx measurements indicated that the tissue would likely be in the dispersion asymptotic regime when glymphatic flow is measured by using a typical DTI protocol. In such a case, the dispersion process reaches a steady state, and measurement results become more reliable.

4. Conclusion

In this study we designed, constructed, and tested a glymphatic transport MRI phantom to assess the feasibility of detecting dispersive mixing behavior using DWI. The measured DTI metrics derived from water flowing at a rate of 0.44 ml/min through the bead layer all greatly increased compared to the stationary case (Tables 1 and 2). Both the transverse and the longitudinal dispersion coefficients were significantly affected. It should be noted that this phantom, which oversimplifies the environment of brain parenchyma, does not contain an intra-cellular region. In reality, the presence of restricted diffusion within the cells, which should be independent of the flow process, is expected to contribute to the diffusion-weighted signal. Nevertheless, the presented results indicate that DTI has the potential to detect dispersive flow within the range of CSF flow rates in human tissue.

Acknowledgements

This work was supported by funds provided by the Intramural Research Program of the *Eunice Kennedy* Shriver National Institute of Child Health and Human Development (grant number ZIAHD000266) and the Center for Neuroregenerative Medicine (CNRM) under the auspices of the Henry M. Jackson Foundation (HJF). The authors thank Ms. Liz Salak for editing the manuscript.

References

[1] Iliff JJ, et al. A paravascular pathway facilitates CSF flow through the brain parenchyma and the clearance of interstitial solutes, including amyloid β. Sci Transl Med 2012;4:147ra111.
[2] Iliff JJ, et al. Brain-wide pathway for waste clearance captured by contrast-enhanced MRI. J Clin Invest 2013;123(3):1299–309.
[3] Iliff JJ, et al. Cerebral arterial pulsation drives paravascular CSF-interstitial fluid exchange in the murine brain. J Neurosci 2013;33(46):18190–9.
[4] Rennels ML, Blaumanis OR, Grady PA. Rapid solute transport throughout the brain via paravascular fluid pathways. Adv Neurol 1990;52:431–9.
[5] Jessen NA, Munk ASF, Lundgaard I, Nedergaard M. The Glymphatic system: a beginner's guide. Neurochem Res 2015;40(12):2583–99.
[6] Xie L, et al. Sleep drives metabolic clearance from the adult brain. Science 2013;342(80):1–11. (no. 6156).
[7] Kress BT, et al. Impairment of paravascular clearance pathways in the aging brain. Ann Neurol 2014;76(6):845–61.
[8] Weller RO, Subash M, Preston SD, Mazanti I, Carare RO. Perivascular drainage of amyloid-β peptides from the brain and its failure in cerebral amyloid angiopathy and Alzheimer's disease. Brain Pathol 2008;18(2):253–66.
[9] Ross CA, Poirier MA. Protein aggregation and neurodegenerative disease. Nat Med 2004;10(7):S10.
[10] Plog BA, et al. Biomarkers of traumatic injury are transported from brain to blood via the glymphatic system. J Neurosci 2015;35(2):518–26.
[11] Sullan MJ, Asken BM, Jaffee MS, DeKosky ST, Bauer RM. Glymphatic system disruption as a mediator of brain trauma and chronic traumatic encephalopathy. Neurosci Biobehav Rev 2018;84:316–24.
[12] Abbott NJ. Evidence for bulk flow of brain interstitial fluid: significance for physiology and pathology. Neurochem Int 2004;45(4):545–52.
[13] Szentistvanyi I, Patlak CS, Ellis RA, Cserr HF. Drainage of interstitial fluid from different regions of rat brain. Am J Physiol Physiol 1984;246(6):F835–44.
[14] Yoffey JM, Courtice FC. Lymphatic, lymph and the lymphomyeloid complex. London: Academic Press; 1970.
[15] Orban BJ, Sicher H. Orban's oral histology and embryology. 5th ed. Saint Louis: C.V. Mosby Co; 1962.
[16] Faghih MM, Sharp MK. Is bulk flow plausible in perivascular, paravascular and paravenous channels? Fluids Barriers CNS 2018;15(1):1–10.
[17] Stejskal EO, Tanner JE. Spin diffusion measurements: spin echoes in the presence of a time-dependent field gradient. J Chem Phys 1965;42(1):288–92.
[18] Callaghan PT, Eccles CD, Xia Y. NMR microscopy of dynamic displacements: k-space and q-space imaging. J Phys E 1988;21(8):820–2.
[19] Basser PJ, Mattiello J, Lebihan D. MR diffusion tensor spectroscopy and imaging. Biophys J 1994;66(1):259–67.
[20] Callaghan PT. Translational dynamics and magnetic resonance: Principles of pulsed gradient spin Echo NMR. New York: Oxford University Press; 2011.
[21] Harrison IF, et al. Non-invasive imaging of CSF-mediated brain clearance pathways via assessment of perivascular fluid movement with DTI MRI. elife 2018;7:1–14.
[22] Von Dem Hagen EAH, Henkelman RM. Orientational diffusion reflects fiber structure within a voxel. Magn Reson Med 2002;48(3):454–9.
[23] Poupon C, Rieul B, Kezele I, Perrin M, Poupon F, Mangin JF. New diffusion phantoms dedicated to the study and validation of high-angular-resolution diffusion imaging (HARDI) models. Magn Reson Med 2008;60(6):1276–83.
[24] Komlosh ME, Özarslan E, Lizak MJ, Horkay F, Schram V, Shemesh N, et al. Pore diameter mapping using double pulsed-field gradient MRI and its validation using a novel glass capillary array phantom. J Magn Reson 2011;208(1):128–35.
[25] Komlosh ME, Benjamini D, Barnett AS, Schram V, Horkay F, Avram AV, et al. Anisotropic phantom to calibrate high-q diffusion MRI methods. J Magn Reson 2017;275:19–28.
[26] Benjamini D, Komlosh ME, Basser PJ. Imaging local diffusive dynamics using diffusion exchange spectroscopy MRI. Phys Rev Lett 2017;118(15).
[27] Bear J. Dynamics of fluids in porous media. Elsevier Inc.; 1972.
[28] Seymour JD, Callaghan PT. Generalized approach to NMR analysis of flow and dispersion in porous media. AICHE J 1997;43(8):2096–111.
[29] Benjamini D, Komlosh ME, Williamson NH, Basser PJ. Generalized mean apparent propagator (GMAP) MRI to measure and image advective and dispersive flows in medicine and biology. IEEE Trans Med Imaging 2018. https://doi.org/10.1109/TMI.2018.2852259.
[30] Khrapitchev AA, Callaghan PT. Reversible and irreversible dispersion in a porous medium. Phys Fluids 2003;15(9):2649–60.